

A comparative study on magnetic order and field-induced magnetic transition in double perovskite iridates: $\text{RE}_2\text{ZnIrO}_6$ and $\text{RE}_2\text{MgIrO}_6$ (RE=Pr,Nd,Sm,Eu,Gd)

Yuxia Gao^{1,2}, Zhaoming Tian^{1,2}[✉], Longmeng Xu^{1,2}, Malik Ashtar^{1,2}, Zongtang Wan^{1,2}, Zhengcai Xia^{1,2}[✉], Feng Yang^{1,2}, Songliu Yuan^{1,2}, Yuyan Han³, Wei Tong³

¹ School of Physics, Huazhong University of Science and Technology, Wuhan 430074, P. R. China

² Wuhan National High Magnetic Field Center, Huazhong University of Science and Technology, Wuhan 430074, P. R. China

³ Anhui Province Key Laboratory of Condensed Matter Physics at Extreme Conditions, High Magnetic Field Laboratory, Chinese Academy of Science, Hefei, 230031, PR China.

Abstract: We perform a comparative magnetic study on two series of rare-earth (RE) based double perovskite iridates RE_2BIrO_6 (RE=Pr,Nd,Sm-Gd;B=Zn,Mg), which show Mott insulating state with tunable charge energy gap from ~ 330 meV to ~ 560 meV by changing RE cations. For nonmagnetic RE=Eu cations, $\text{Eu}_2\text{MgIrO}_6$ shows antiferromagnetic (AFM) order and field-induced spin-flop transitions below Néel temperature (T_N) in comparison with the ferromagnetic (FM)-like behaviors of $\text{Eu}_2\text{ZnIrO}_6$ at low temperatures. For magnetic-moment-containing RE ions, Gd_2BIrO_6 show contrasting magnetic behaviors with FM-like transition (B=Zn) and AFM order (B=Mg), respectively. While, for RE=Pr, Nd and Sm ions, all members show AFM ground state and field-induced spin-flop transitions below T_N irrespective of B=Zn or Mg cations. Moreover, two successive field-induced metamagnetic transitions are observed for $\text{RE}_2\text{ZnIrO}_6$ (RE=Pr,Nd) in high field up to 56 T, the resultant field temperature (H - T) phase diagrams are constructed. The diverse magnetic behaviors in RE_2BIrO_6 reveal that the $4f$ -Ir exchange interactions between the RE and Ir sublattices can mediate their magnetism.

Keywords: antiferromagnetic, ferromagnetic, spin flop, Mott insulator

1. Introduction

The 5d iridates have attracted great attention as candidate materials for exploring exotic quantum phases of matter with unconventional electronic and magnetic ground

[✉] Author to whom correspondence should be addressed: tianzhaoming@hust.edu.cn

[✉] xia9020@hust.edu.cn

states, such as novel Mott insulator [1], Kitaev spin liquid [2], Weyl semimetal [3,4] and even unconventional superconductors [5]. The underlying mechanisms of these exotic phenomena are associated with strong spin-orbital coupling (SOC) and its interplay with large crystalline electric fields (CEF), electron correlation interactions (U) in comparable energy scales. As one prominent consequence of strong SOC in iridates, it leads to the formation of so-called novel “ $j_{\text{eff}}=1/2$ Mott insulator” as initially discovered in Sr_2IrO_4 compound [6]. Within this picture, the energy scale of competitive SOC, CEF and electron correlation interactions can be substantially tailored by local environment, symmetry or dimensionality [7,8], which can modify or even destroy the $j_{\text{eff}}=1/2$ state. In this respect, iridates with different lattice geometries or spin-exchange pathways provide template to explore diverse exotic quantum states. A variety of systems with different geometrical structure have been garnered considerable interest, such as the perovskite Sr_2IrO_4 and SrIrO_3 [6,9], honeycomb compounds Na_2IrO_3 and Li_2IrO_3 [10,11], hyperkagome $\text{Na}_4\text{Ir}_3\text{O}_8$ [12] and pyrochlore iridates $\text{RE}_2\text{Ir}_2\text{O}_7$ (RE=rare earth) [13], etc.

Recently, the ordered double perovskite (DP) iridates with chemical formula A_2BIrO_6 (A is rare earth ions, B is 3d transition metal or alkaline earth metal) become intensively studied as a new system of “ $j_{\text{eff}}=1/2$ Mott insulator” [14-16]. In this family, large space separated Ir ions displaying a “rock-salt” face-centered-cubic (FCC) symmetry, lets this system have new features beyond ABO_3 perovskites such as geometric spin frustration, weakened direct Heisenberg exchange, enhanced SOC effect or even emergence of Kitaev interactions [17,18]. In case of nonmagnetic A/B cations (A=La,Y; B=Zn,Mg), A_2BIrO_6 is a prototypical compound where magnetism is dictated by 5d electrons of Iridium. When A site is occupied by magnetic rare-earth (RE) cations (A=Pr,Nd,etc), the 4f-4f exchange interactions within RE ions at A sites exist, also the 4f-Ir exchange interactions between the A/B sublattices are possibly present. In this case, the 4f magnetic moments together with 4f-Ir interaction as additional term coupled to the Ir^{4+} moments will enrich its magnetic and electronic behaviors, while the related issue is unclear.

Experimentally, the basic magnetic properties of $\text{RE}_2\text{MgIrO}_6$ (RE=La,Pr,Nd,Sm-Gd) compounds were previously characterized [19,20], most of them show antiferromagnetic (AFM) order. The recent studies reveal that the RE_2BIrO_6 (RE=La,Eu) with nonmagnetic A cations show disparate magnetic orders in respect to B=Mg or Zn [14,21,22], where $\text{RE}_2\text{ZnIrO}_6$ but not $\text{RE}_2\text{MgIrO}_6$ show ferromagnetic (FM)-like hysteresis below Curie temperature (T_C) [14,22]. While, as RE is extended to magnetic-moment-contained ions, their magnetic behaviors are still controversial, as example, the recent experimental studies on Sr-doped $\text{Pr}_2\text{MgIrO}_6$ show they are neither half-metallicity nor long-range ferrimagnetic ordering [23], sharply contrast to the theoretically predicted half-metallic antiferromagnetism/ferrimagnetism [24]. Moreover, very recent Raman scattering measurements reveal the existence of fractionalized excitations in $\text{Sm}_2\text{ZnIrO}_6$ [25],

supporting its' possible spin liquid state. Thus, to clarify their controversial magnetic behaviors in RE_2BIrO_6 , further studies are highly desirable.

Here, we report a comparative study on magnetic behaviors and field-induced magnetic transitions in two serial RE_2BIrO_6 ($\text{RE}=\text{Pr},\text{Nd},\text{Sm},\text{Eu},\text{Gd}$; $\text{B}=\text{Zn},\text{Mg}$) double perovskite iridates, our electrical measurements show all members have Mott insulating states with tunable charge gap from ~ 330 meV to ~ 560 meV as changing RE from La to Gd. In case of $\text{RE}=\text{Eu},\text{Gd}$, $\text{RE}_2\text{MgIrO}_6$ exhibit the AFM order and field induced spin flop transitions below Néel temperature (T_N) in comparison with the FM order with typical FM hysteresis of $\text{RE}_2\text{ZnIrO}_6$. As for $\text{RE}=\text{Pr}, \text{Nd}$ and Sm , all compounds exhibit field induced spin-flop transitions below T_N . Moreover, two successive field induced metamagnetic transitions are observed for $\text{RE}_2\text{ZnIrO}_6$ ($\text{RE}=\text{Pr},\text{Nd}$) under field up to 56 T, and the magnetic field temperature (H - T) phase diagrams are constructed.

2. Experiment

Two serial RE_2BIrO_6 ($\text{RE}=\text{La},\text{Pr},\text{Nd},\text{Sm},\text{Eu},\text{Gd}$; $\text{B}=\text{Zn},\text{Mg}$) polycrystals were synthesized by conventional solid state reaction method. The mixtures were prepared using rare-earth oxides (99.99% RE_2O_3 for $\text{RE}=\text{La},\text{Nd},\text{Sm},\text{Eu}$ and Gd ; 99.9% Pr_2O_3) ZnO (99.9%), MgO (99.5%) and IrO_2 (Tanaka Kikinokogyo) as starting materials. For the RE_2BIrO_6 ($\text{RE}=\text{La}, \text{Pr},\text{Nd},\text{Sm}$) samples, stoichiometric mixtures were carefully ground and reacted at temperature of 1150°C in air for 4 days with intermediate grindings. For $\text{RE}=\text{Eu},\text{Gd}$ compounds, higher reaction temperature of 1200°C - 1250°C is required to obtain pure phase sample. The attempts to synthesize the compounds with smaller size cations than $\text{RE}=\text{Tb}$ by different heating procedures at ambient pressure were unsuccessful. Additionally, to analyze magnetic behaviors of Eu_2BIrO_6 , isostructural Eu_2BTiO_6 compounds were also synthesized using similar heating sequences. The structure and phase purity were checked by the X-ray diffraction (XRD, Rigaku Smartlab) measurements with $\text{Cu K}\alpha$ radiation ($\lambda=1.5418\text{\AA}$). To get the structural parameters, the XRD spectra were analyzed through Rietveld refinements using the material studio software.

Magnetic measurements were carried out by the superconducting quantum interference device magnetometer (SQUID, Quantum Design) and commercial Physical Property Measurement System (PPMS, Quantum Design) with a vibrating sample magnetometry (VSM) option in applied DC magnetic fields up to 14 T, including temperature dependent susceptibility from 2 K-300 K and isothermal field dependent magnetization $M(H)$ measurements. The electrical resistance was measured by a standard four-probe method. The pulsed field magnetizations up to 56 T were measured by the induction method at Wuhan National High Magnetic Field Centre (WHMFC) down to 2 K with a calibration by the DC magnetization data.

3. Results and Discussions

3.1 Structural analysis of RE₂BIrO₆

The double perovskite (DP) RE₂BIrO₆ crystallize into monoclinic structure with space group $P2_1/n$, as report in RE₂MgIrO₆ (RE=La-Nd,Sm-Gd) [19-20]. This space group allows for two crystallographically distinct octahedral sites in the double perovskite structure, the BO₆ and IrO₆ octahedras are ordered in a rock-salt manner and their tilting to accommodate the small size RE cations. As a representative, the crystal structure of Pr₂ZnIrO₆ is presented in figure 1(a), with Pr atoms at 4e(x y z) positions, Zn at 2c (0 0 0) positions, Ir at 2d (1/2 1/2 0) and three types of oxygen atoms at 4e(x y z) sites. Within the corner-shared connections of ZnO₆/IrO₆ octahedras, the Pr³⁺ cations fit the distorted cubic network of these rock-salt lattices in the local coordination environment of Ir⁴⁺/Pr³⁺ atoms, as shown in figure 1(b,c). The Pr³⁺ atom is coordinated by eight oxygen atoms, forming the irregular Pr³⁺-O polyhedron with different Pr³⁺-O bond lengths. Each Ir⁴⁺ atom is surrounded by eight nearest-neighboring Pr³⁺ atoms, the Ir⁴⁺-O bond distance varies within an octahedron, where six Ir-O bond lengths are grouped into three values reflecting the octahedral distortions.

The powder X-ray diffraction (XRD) spectra are refined by Rietveld methods, which reveal all RE₂BIrO₆ (RE= La,Pr,Nd,Sm,Eu,Gd) compounds are single phase without detected phase impurities. The resultant structural parameters for RE₂ZnIrO₆ are shown in figure 2(a), where the lattice parameters a and c show regularly decrease with radius size of rare earth (RE) cations, in comparison with the slightly increase of b parameter. Similar trends for RE₂MgIrO₆ are also observed as report in Ref [19]. This behavior can be related to the tilting scheme of ZnO₆ and IrO₆ octahedra in the $P2_1/n$ space group, corresponding to the $a^-a^+b^+$ in the Glazer's notation [26]. In this tilting system, structural distortion driven by the reduction of RE³⁺ will cause minimal modification of the b parameter. For the octahedral distortion in RE₂BIrO₆, it can be identified by the distorted B-O-Ir bond angle away from ideal 180°. The tilting of (B,Ir)O₆ octahedra is characterized by the average tilting angle defined as $\phi = (180 - \omega) / 2$, where ω is the inter-octahedral B-O-Ir angle. In figure 2(b), the evolution of average tilting angle (ϕ), the RE-O and Ir-O bond lengths are presented, it is noted that smaller RE-ion radius cause larger tilting angles from La³⁺ to Gd³⁺, namely larger monoclinic distortions. In terms of interatomic distances, the size of RE³⁺ ions mainly affects the average <RE-O> bond lengths, which almost linearly correlate with the RE³⁺ radius, but no systematic change of <Ir-O> average lengths are detected in these series.

3.2 Electrical transport of RE₂BIrO₆

Figures 3(a,b) show the temperature (T) dependence of electrical resistivity $\rho(T)$ for

RE₂BIrO₆ (B=Zn, Mg), respectively. For all compounds, a monotonic increase in $\rho(T)$ as decreased T reveals the insulating ground state. Among the families, the $\rho(T)$ of compounds with smaller RE ionic radius show larger resistance over all temperatures. As shown in figures 3(c) and (d), the experimental data are fitted by the thermal activation model described by $\rho(T) = \rho_0 \exp(\Delta / 2k_B T)$, where Δ is the activation energy and k_B is the Boltzmann constant. At higher temperatures, the resistivity follows the thermally activation model, but it deviates as decreased temperatures. The estimated charge energy gaps (Δ) in temperature regions 270 K-350K are listed in Table 1, which varies from ~336 meV (RE=La) to ~517 meV (RE=Gd) for RE₂ZnIrO₆. The Mg-containing analogs display similar trend with relatively larger charge gaps. Additionally, the $\rho(T)$ data can be better described by a three dimensional (3D) Mott variable-range-hopping (VRH) model [27]: $\rho = \rho_0 \exp\left(\frac{T_0}{T}\right)^{1/4}$, where ρ_0 is the resistivity coefficient and T_0 is the localization temperature. This is indicated by the straight line fit of $\ln\rho$ versus $T^{-1/4}$ in figures 3(e) and (f)]. The fitted parameters T_0 are given in Table 1. According to the VRH model, T_0 depends on the localization length l and the density of states at the Fermi level $N(E_F)$ in a relation of $T_0 = 18 / k_B N(E_F) l^3$ [28]. Then, the electron hopping between the localized states can be responsible for the electrical conductivity, the increase of T_0 as changing RE from La³⁺ to Gd³⁺ can be related to the increased l . The 3D character in the electronic transport is reasonable since the building blocks are made of well-separated IrO₆ octahedrons with FCC-type arrangement of Ir⁴⁺ lattice, the large space separated Ir ions and electron correlations may account for the charge localizations. Similar transport mechanisms were reported in other 5d DP oxides Sr₂InReO₆ and Ba₂NaOsO₆ [29,30]. In all, the $\rho(T)$ curves reveal RE₂BIrO₆ have charge-gapped Mott insulating states, the gap size can be tuned in a range from ~330 meV to 560 meV by changing RE ions.

3.3 Magnetic behaviors of RE₂BIrO₆

The zero-field-cooled (ZFC) and field-cooled (FC) magnetic susceptibilities $\chi(T)$ were measured under field $H = 0.1$ T for RE₂BIrO₆, which are shown in figure 4(a)-(e), respectively. For RE=Pr,Nd and Sm, $\chi(T)$ for both B=Zn and Mg compounds show antiferromagnetic (AFM) transition at Néel temperature T_N . Below T_N , no distinct divergences are observed between the ZFC and FC magnetizations. As shown in figure 4(f)-(h), the inverse susceptibility $1/\chi(T)$ at paramagnetic (PM) states are fitted by the Curie-Weiss (CW) Law: $\chi(T) = \frac{C}{T - \theta_{CW}}$, where C is the Curie constant and θ_{CW} is the Curie-Weiss temperature. For Sm₂BIrO₆, we fit $1/\chi(T)$ at low temperature region (30 K-70 K) since the Sm³⁺ ions have high temperature Van-Vleck paramagnetic (PM) contributions

[31], leading to its' deviation of linear dependence. The fitted θ_{CW} and effective magnetic moments (μ_{eff}) are summarized in Table 2. Large negative θ_{CW} compared to T_N , as example, $\theta_{CW} = -53.3$ K around 4 times large of T_N for $\text{Pr}_2\text{ZnIrO}_6$, indicates the presence of magnetic frustration. The derived experimental moments are close to the theoretical value

$$\mu_{eff} = \sqrt{2\mu_{RE}^2 + \mu_{Ir}^2} \quad \text{with combinations of the moments of free RE}^{3+} \text{ ion}$$

$$\mu_{RE} = g_J[J(J+1)]^{1/2} \text{ and } \mu_{Ir} = 2[1/2(1/2+1)]^{1/2} = 1.73\mu_B/\text{Ir}^{4+}.$$

As shown in figure 4(d), $\text{Eu}_2\text{ZnIrO}_6$ shows ferromagnetic (FM)-like transition with $T_C \sim 11$ K, below which the ZFC and FC magnetizations show large bifurcations. The FM-order state is further confirmed by the FM-like hysteresis below T_C [see figure 5(a)]. In contrast, $\text{Eu}_2\text{MgIrO}_6$ shows AFM-type transition with $T_N \sim 10.4$ K. Since the Eu^{3+} ions (${}^7F_0, 4F_6$, $S=3$, $L=3$, $J=0$) possess no magnetic moment and the excited states 7F_J ($J=1, 2, \dots$) only give rise to weak temperature dependent Van-Vleck PM contribution [32], low temperature magnetic orders are dictated by the Ir^{4+} moments in Eu_2BIrO_6 . So, to quantatively evaluate their magnetic interactions, the Van-Vleck PM contribution (χ_{VV}) from Eu^{3+} ions should be subtracted [33]. Here, the susceptibility of isostructural Eu_2BTiO_6 ($B=\text{Zn, Mg}$) is used as χ_{VV} (see Appendix, figure 11), the yielded $1/\chi_{Ir} = 1/(\chi - \chi_{VV})$ is presented in figure 4(i). From the CW fitting, the obtained $\theta_{CW} = 9.4$ K (Zn) and -15.3 K (Mg) reveal its dominant FM and AFM interactions, respectively.

To more clearly characterize the ferromagnetism in $\text{Eu}_2\text{ZnIrO}_6$, the Arrott analysis is used to determine the T_C and ordered moment. As shown in figure 5(b), we show $(M)^{1/\beta}$ versus $(H/M)^{1/\gamma}$ plots. At 11 K, the isothermal magnetization has a linear dependence with $\beta=0.65$ and $\gamma=1.21$, which correct $T_C=11$ K. The saturated magnetization (M_S) at 2 K is determined to $0.37\mu_B/\text{Ir}$ from linear extrapolation of the straight line in modified Arrott plots. Under high field, its magnetization has linear field dependence without saturation up to 56 T (see figure 5(c)), this can be due to the dominant Van-Vleck PM contributions persistent up to high fields.

The isothermal magnetization $M(H)$ curves of $\text{Eu}_2\text{MgIrO}_6$ are shown in figure. 6(a). Below T_N , the $M(H)$ show pronounced steepening near critical field (H_C) featured a field-induced spin-flop transition, different from the FM hysteresis behaviors of $\text{Eu}_2\text{ZnIrO}_6$. Here, H_C is defined by the peak position of derivative magnetization dM/dH , as shown in the figure 6(b). The H_C decreases with increased temperatures towards zero at T_N . From the magnetic susceptibilities at different fields, the $\chi(T)$ shows a peak at T_N as $H < 3$ T, further increased H , the peak becomes broadened and gradually smeared out. In this case, T_N is defined by the peak of derivative dM/dT as shown in the inset of figure 5(c). Based on above $M(H)$ and $\chi(T)$ data, a schematic magnetic field/temperature (H - T) phase diagrams are constructed, shown in figure 6(d). The presence of spin flop reveals the evolution of magnetic structures from AFM to canted-antiferromagnetic (C-AFM) states.

The linear extrapolation of high field magnetization at 2 K yields net remnant magnetization $\sim 0.27\mu_B/\text{f.u.}$, this indicates $\text{Eu}_2\text{MgIrO}_6$ have C-AFM phase with net FM moments above H_C .

As presented in figure 4(e), Gd_2BIrO_6 (B=Zn,Mg) show distinct magnetic behaviors, $\text{Gd}_2\text{ZnIrO}_6$ shows FM-like behavior supported by the steep increase of FC magnetization near $T_C\sim 22$ K and well-shaped FM hysteresis below T_C (See figure 7(a)). While, $\text{Gd}_2\text{MgIrO}_6$ exhibits the AFM-like transition with $T_N\sim 20.8$ K, where T_N is defined by the peak of derivative dM/dT [see the inset of figure 7(c)]. Moreover, different sign of θ_{CW} with $\theta_{\text{CW}}=1.5$ K (B=Zn) and $\theta_{\text{CW}}=-5.3$ K (B=Mg) also support the different dominant FM or AFM interactions, respectively. For $\text{Gd}_2\text{ZnIrO}_6$, the remnant magnetization $M_r=2.52\mu_B/\text{f.u.}$ at 2 K is much larger than the maximum value $M_S=1.0\mu_B/\text{Ir}^{4+}$, this imply that the Gd^{3+} moments have FM contributions. As a comparison, this typical FM behaviors are contrast to magnetic behaviors reported quite recently in $\text{Gd}_2\text{ZnIrO}_6$, where it exhibits wasp-waist-like hysteresis and small remnant magnetization ($M_r\sim 1.5\mu_B/\text{f.u.}$) [22]. As shown in the inset of figure 7(a), its magnetization saturates at ~ 20 T with $M_S=14.8\mu_B/\text{f.u.}$, this value is consistent with the theoretical saturated moments $= (2g_JJ_{\text{Gd}} + g_{\text{Ir}}J_{\text{Ir}})\mu_B/\text{f.u.} = (2\times 2\times \frac{7}{2} + 2\times \frac{1}{2})\mu_B/\text{f.u.} = 15\mu_B/\text{f.u.}$ for combinations of 2Gd^{3+} and Ir^{4+} moments. For $\text{Gd}_2\text{MgIrO}_6$, $M(H)$ curves show waist-restricted shape hysteresis with nearly zero remnant magnetization. This unusual hysteresis reveal the field induced spin-flop transition from the magnetic reorientation of Gd^{3+} and Ir^{4+} sublattices, the resultant H - T phase diagrams are shown in figure 6(d). Compared to $\text{Eu}_2\text{MgIrO}_6$, the smaller $H_C\sim 0.8$ T at 2 K can be related to the large gained Zeeman energy of Gd^{3+} spins coupled to external fields. Moreover, since the Gd^{3+} moments ($7.94\mu_B/\text{Gd}^{3+}$) is much larger than Ir^{4+} moments ($1.73\mu_B/\text{Ir}^{4+}$), the monotonically increased magnetization at high fields in Gd_2BIrO_6 can be attributed to the alignment of Gd^{3+} moments.

For RE_2BIrO_6 (RE=Pr,Nd, Sm; B=Zn,Mg), the isothermal DC magnetization curves at 2 K are shown in figure 8(a),(c) and (e), respectively. At low fields, linear dependent magnetization behaviors are in consistent with their AFM ground states. Further increased field, a field induced spin-flop transitions appear, the small hysteresis indicates the characteristic of 1st order transition, as also seen from the dM/dH curves in the inset of figure 8(a). To further identify the field-induced metamagnetic transitions, pulsed field magnetization measurements up to 56 T are shown in figure 8(b),(d) and (f). As seen, the 2nd metamagnetic transition occurs for $\text{RE}_2\text{ZnIrO}_6$ (RE=Pr,Nd), where another anomaly of dM/dH appears near H_{c2} [see the inset of figure 8(b) and (d)]. While for Mg-analogues, no 2nd field-induced transitions are detected. Here, the observed metamagnetic transitions reveal the existence of spin-reorientation of the $\text{Pr}^{3+}/\text{Nd}^{3+}$ and Ir^{4+} moments. Additionally, the saturated magnetization moment (M_S) at 56 T is far below the theoretical saturation

moment value $M_S=2M_{RE}+M_{Ir}$, as example, the experimental $M_S\sim 3.49\mu_B/f.u.$ for Pr_2ZnIrO_6 is quite smaller than expected $M_S=(2g_JJ+1)\mu_B/f.u.= (2\times 0.8\times 4+1)\mu_B/f.u.= 7.4\mu_B/f.u.$ This can be related to the reduced moments of Pr^{3+}/Nd^{3+} at low temperatures due to the low-lying CEF effects [34,35]. Further taking into account its Ising-like magnetic anisotropy, the saturated magnetization per Pr^{3+} ions should be $g_JJ/2 \sim 1.15-1.3\mu_B$, then the yielded $M_S=(2\times \frac{1}{2}g_JJ+1)\mu_B \sim 3.3-3.6\mu_B$ agrees well with our experimental value. Here, the used moment of Pr^{3+} is consistent with the detected moment value ($2.3\mu_B$) by neutron powder diffraction in the isostructural Pr_2LiRuO_6 system [36]. For Sm_2ZnIrO_6 , high-field magnetizations show no sign of saturation up to 56 T, its maxima moment $\sim 1.2\mu_B/f.u.$ is far from saturated value in respect to effective moments $\sim 0.85\mu_B/Sm^{3+}$ and $1.73\mu_B/Ir^{4+}$. Thus, no 2nd metamagnetic transition is detected possibly because the H_{C2} is beyond our measured field regions.

For Pr_2ZnIrO_6 , the isothermal magnetization curves for field sweep-up branches under DC and pulsed magnetic fields are shown in figure 9(a) and (c), field-induced two successive metamagnetic transitions are detected below T_N . The evaluated H_{C1} from the peak position of dM/dH curves decreases as increased temperatures (see figure 9(b)). In figure 9(d), we present the magnetic susceptibilities measured at different fields. T_N is defined by the peak of derivative dM/dT , as shown in the inset of figure 9(d). Using the H_C and T_N obtained from above $M(H)$ and $M(T)$ data, the H - T phase diagram of Pr_2ZnIrO_6 is constructed, as shown in figure 10(a). Similar H - T phase diagram of Nd_2ZnIrO_6 is also mapped based on high field magnetization curves (see Appendix, figure 12), as shown in figure 10(b). At low temperatures, The H_{C1} for field sweep-up and field sweep-down are different as shown in figure 8, as characteristics of 1st order transition. Above 7 K, the magnetization for field sweep-up and sweep-down completely overlaps. To better understand this transition, we do a linear magnetization extrapolation as show in in figure 8(a),(c) and (f). Considering that the saturated moment $\sim 0.27-0.37 \mu_B/Ir^{4+}$ in A_2ZnIrO_6 ($A=La,Eu$) [14,37], different yielded magnetization values of $0.92 \mu_B/f.u.$ ($A=Pr$), $1.12\mu_B/f.u.$ (Nd) and $0.17\mu_B/f.u.$ ($A=Sm$) reveal its origin from the spin-reorientation of RE^{3+} moments. Above H_{C1} , the RE^{3+} sublattices form a C-AFM ordered state with net FM components. Additionally, the 2nd metamagnetic transition observed at high field for $B=Zn$ instead of Mg-analogues reveal the existence of different magnetic configurations for Zn/Mg series at high fields.

3.4 Discussions

Among the DP iridates, magnetic behaviors of A_2BIrO_6 ($A=La,Eu$) are dictated by the Ir^{4+} ($j_{eff}=1/2$) moment on the face-centered-cubic (FCC) lattices. From the structural analysis, the IrO_6 octahedron in A_2BIrO_6 series has a rotation ϕ relative to c axis. In strong spin-orbital coupled (SOC) limit, Ir moments can be rigidly locked to the octahedral

rotation. In this case, this octahedral rotations can induce a collective deviation of $j_{\text{eff}}=1/2$ moment canted away from [110] axis in the ab plane, as revealed by recent neutron powder diffractions and theoretical analysis in La_2BIrO_6 [17,18], where the Ir^{4+} moments form A-type AFM ground state, but have different magnetic configurations in respect to $\text{B}=\text{Zn}^{2+}$ or Mg^{2+} ions. In $\text{La}_2\text{ZnIrO}_6$, the Ir^{4+} moments prefer FM coupling within the ab plane and staggered AFM between the adjacent ab layers [17]. In this spin arrangement, net FM moments can arise from the isospin canting effect determined by the staggered rotation angle (ϕ), similar spin configurations should also be formed in $\text{Eu}_2\text{ZnIrO}_6$ responsible for appearance of net FM moments. While, in A_2MgIrO_6 ($\text{A}=\text{La},\text{Eu}$), the FM planes are in the xz planes and stack AFM along y axis, so no net FM moment is obtained. The observed spin flops in $\text{Eu}_2\text{MgIrO}_6$ reflect the evolution of magnetic structures from AFM to C-AFM state, above H_C , the C-AFM phase has net FM moments.

For compounds containing magnetic 4f RE ions, the introduced RE ions can dramatically alter their magnetic behaviors. For larger size RE cations ($\text{RE}=\text{Pr}, \text{Nd}$ and Sm), all members of two branches show AFM ground state and field induced metamagnetism, but Gd_2BIrO_6 ($\text{B}=\text{Mg},\text{Zn}$) resemble magnetic features as observed in A_2BIrO_6 ($\text{A}=\text{La},\text{Eu}$) analogs with FM ($\text{B}=\text{Zn}$) and AFM ($\text{B}=\text{Mg}$) ordered states, respectively. The above diverse magnetic behaviors cannot solely be attributed to the exchange coupling of Ir^{4+} sublattices, the intra-sublattice RE-RE exchange interaction and inter-sublattice 4f-Ir exchange couplings should be included. Among RE^{3+} ions, Gd^{3+} is special and has half-filled 4f shell ($4f^7$, $S=7/2$, $L=0$), which usually show quasi-isotropic magnetic interactions due to the absence of CEF effect. This is relatively simple compared to other RE^{3+} -based systems, where magnetic anisotropy is also affected by the CEF splitting. Given that the absence of Gd-Ir magnetic couplings, the Gd-Gd magnetic correlations should occur at much lower temperatures ~ 1 K [38]. Here, Gd_2BIrO_6 show highest transition temperatures (~ 20 K) accompanied by enhanced magnetizations, indicative of the ordering of Gd^{3+} magnetic sublattices below T_N or T_C via the Gd-Ir coupling. The Gd-Ir exchange interactions can be produced by the four first-neighbor Ir^{4+} of each Gd^{3+} site, and the Gd^{3+} spins show some similar features of Ir^{4+} sublattices with compatibility. This can explain the resemblance of magnetic behaviors in Gd_2BIrO_6 compared to its Eu_2BIrO_6 counterparts. $\text{Gd}_2\text{ZnIrO}_6$ has FM hysteresis with larger FM component $M_S=4.2(2)\mu_B/\text{f.u.}$ at 2 K, $\sim 28\%$ of its saturated moments ($M_S=15\mu_B/\text{f.u.}$), signify the ferromagnetically coupled Gd^{3+} and Ir^{4+} sublattices.

As for $\text{RE}=\text{Pr}, \text{Nd}$ and Sm , all members of RE_2BIrO_6 share AFM ground state without FM components irrespective of $\text{B}=\text{Zn}$ or Mg , this is sharply contrast to the Gd counterpart. Moreover, the large negative θ_{CW} with a moderate frustrated factor, signify the presence of short range AFM correlation above T_N . Here, it should be noted that this AFM order can't be ascribed to either the RE-RE coupling or Ir-Ir interactions along, since the RE-RE

interactions alone are weak, as example, the isostructural $\text{RE}_2\text{LiIrO}_6$ show no magnetic order down to 2 K [39]. Also, the dominant Ir-Ir interactions alone will lead to distinct FM (B=Zn) and AFM (B=Mg)-like behaviors as observed in the RE=La and Eu systems. In this respect, the incorporated RE sublattices seem to destroy the delicate balance of different Ir-Ir exchange interactions for B=Mg or Zn, respectively. The observed metamagnetic transitions in RE_2BTiO_6 (RE=Pr,Nd, Sm) correspond to the spin-flop transition from AFM to C-AFM state. For $\text{Nd}_2\text{ZnIrO}_6$, quite recent neutron diffraction reveals Nd^{3+} moments have AFM state, where magnetic propagation vector along $(1/2\ 1/2\ 0)$ at zero field [22]. As field above H_{C1} , further increased magnetizations favor the C-AFM state. This is consistent with canted antiferromagnetism, where the increased spin-tilting along field direction happens with increased fields. So, the 1st metamagnetic transition should originate from the spin-flip of RE^{3+} sublattices. For $\text{RE}_2\text{ZnTiO}_6$ (RE=Pr,Nd), the 2nd metamagnetic transitions reveals another spin-reorientation of magnetic sublattices, then become the full polarized FM state (PS) at high fields ($H > 40$ T), as illustrated in the H - T phase diagrams.

Compared with spin-only Gd^{3+} ions, the main difference for RE=Pr,Nd and Sm is the presence of orbital moments and substantial CEF, which can tune the exchange interactions between Ir^{4+} and RE^{3+} moments in the exchange path by orbital hybridization. Additionally, three interactions including intra-sublattice Ir-Ir, RE-RE interaction and inter-sublattice RE-Ir exchange coupling are coexistent, all of them can play a role but the relative strength and sign of above interactions can strongly affect its' magnetic behaviors. Similar phenomena have been well reported in RE-based pyrochlore iridates, where the 4f-Ir coupling can dramatically tune their magnetic and electronic properties [40-42]. So, the RE-Ir exchange interactions in RE-based DP iridates provide alternative route to produce new emergent magnetic phases.

4. Conclusions

We performed the comparative study of magnetic order and field-induced metamagnetic transitions on two serial RE-based DP iridates $\text{RE}_2\text{B}^{\text{Ir}}\text{O}_6$ (A=Pr,Nd,Sm-Gd;B=Zn,Mg), which show Mott insulating state with charge energy gap from 330 meV to 560 meV with the variation of RE ions. In case of nonmagnetic RE=Eu cations, $\text{Eu}_2\text{MgIrO}_6$ exhibits AFM ground state and a field-induced spin flop transition from AFM to C-AFM states below T_N , in contrast to the FM behaviors of $\text{Eu}_2\text{ZnIrO}_6$. For magnetic-moment-containing RE cations, the AFM-ordered $\text{Gd}_2\text{MgIrO}_6$ show field-induced spin-flop transition compared to the well-shaped FM hysteresis of $\text{Gd}_2\text{ZnIrO}_6$ below T_C . While, for RE=Pr, Nd and Sm, both Zn- and Mg-branches share similar AFM magnetic ground state and field induced metamagnetic transitions. Finally, two successive field-induced metamagnetic transitions are detected in high magnetic field up to 56 T and resultant magnetic phase diagram are constructed for both $\text{Pr}_2\text{ZnIrO}_6$ and $\text{Nd}_2\text{ZnIrO}_6$

compounds.

During the writing of the present manuscript, we became aware of another study investigating the magnetic properties of serial $\text{RE}_2\text{ZnIrO}_6$ ($\text{RE}=\text{Nd}, \text{Sm}, \text{Eu}, \text{Gd}$) compounds conducted by Vogl M *et al.* [22] Based on high field magnetization measurements with field to ~ 56 T, our work showed the distinct magnetic behaviors and field-induced magnetic transitions in two serial RE_2BIrO_6 compounds. This also allowed us to construct the H - T phase diagrams for the metamagnetic transitions in $\text{RE}_2\text{ZnIrO}_6$ ($\text{RE}=\text{Pr}, \text{Nd}$). We have compared the present magnetic behaviors with their results in the main context.

Conflicts of interest

There are no conflicts to declare.

Acknowledgements

We acknowledge financial support by the National Natural Science Foundation of China (Grant Nos. 11874158 and 11674115), and by fundamental research funds for the central universities (Grant No. 2018KFYXJJ038 and 2019KFYXKJC008). We would like to thank the staff of the analysis center of Huazhong University of Science and Technology for their assistance in various measurements.

Appendix

1. The analysis of magnetic susceptibilities of Eu_2BIrO_6 ($\text{B}=\text{Zn}, \text{Mg}$)

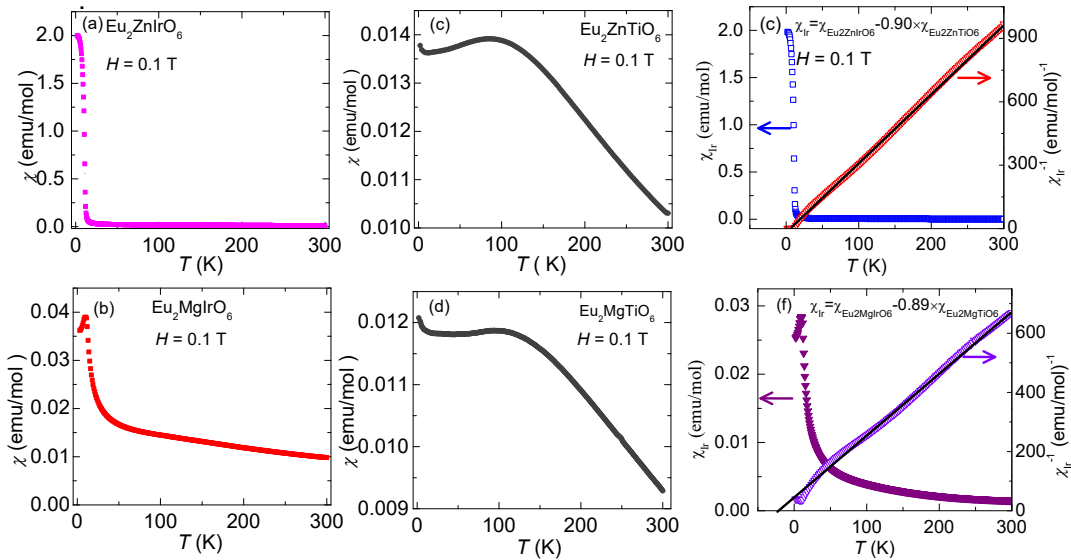


Figure 11. Temperature dependence of magnetic susceptibilities under $H=0.1$ T for (a) $\text{Eu}_2\text{ZnIrO}_6$, (b) $\text{Eu}_2\text{MgIrO}_6$, (c) $\text{Eu}_2\text{ZnTiO}_6$ and (d) $\text{Eu}_2\text{MgTiO}_6$, respectively. The resultant magnetic susceptibilities (χ_{Ir}) and inverse magnetic susceptibilities ($1/\chi_{\text{Ir}}$) for (e) $\text{Eu}_2\text{ZnIrO}_6$ (f) $\text{Eu}_2\text{MgIrO}_6$, the black line shows the linear Curie-Weiss fitting.

Temperature dependence of magnetic susceptibility of Eu_2BIrO_6 (B=Zn,Mg) under $H=0.1$ T are shown in figure 11(a,b). At high temperatures, the inverse susceptibility violates the Curie-Weiss law due to the presence of Van-Vleck paramagnetic (PM) contributions from Eu^{3+} ($L=3, S=3, J=0$) ions [32,33], where electron occupations at excited states can give temperature-dependent contribution to susceptibility at high-temperatures. In this case, high temperature $\chi(T)$ for Eu_2BIrO_6 should include two PM components from both Ir^{4+} and Eu^{3+} sublattices, as shown in figure 11(a) and (b). In this case, we analyze it by a modified Curie-Weiss Law as below: $1/\chi = 1/(\chi_{\text{Ir}} + \chi_{\text{VV}})$, where χ_{Ir} and χ_{VV} are magnetic components from Ir^{4+} and Eu^{3+} sublattices, respectively. To evaluate the magnetic interactions between Ir^{4+} moments, the Van-Vleck PM part (χ_{VV}) is subtracted from the $\chi(T)$ by using the susceptibility of Eu_2BTiO_6 (B=Zn,Mg) [see Figure 11(c) and (d)]. Here, Eu_2BTiO_6 have isostructural to the Eu_2BIrO_6 . The resultant χ_{Ir} and $1/\chi_{\text{Ir}} = 1/(\chi - \chi_{\text{VV}})$ are shown in figure 11(e,f), respectively. From high temperature (180K–300 K) Curie-Weiss fitting, the obtained $\theta_{\text{CW}}=9.4$ K (Zn) and $\theta_{\text{CW}}=-15.3$ K (Mg) reveal its dominant FM and AFM interactions, respectively

2. High field magnetizations of $\text{Nd}_2\text{ZnIrO}_6$

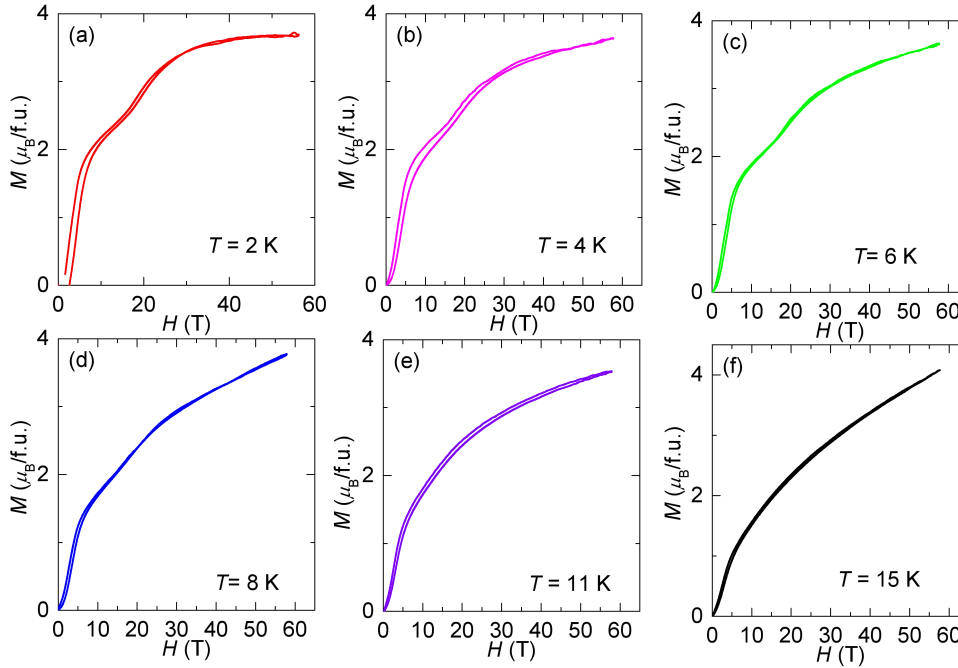


Figure 12. The field dependence of magnetizations with field up to 56 T at different temperatures for $\text{Nd}_2\text{ZnIrO}_6$.

The field dependent magnetization curves of $\text{Nd}_2\text{ZnIrO}_6$ are measured at different temperatures from 2 K to 15 K, the selected $M(H)$ curves are shown in figure 12. Below T_N , the field dependent magnetizations show two successive metamagnetic transitions, where the critical field ($H_{\text{C}2}$) is determined from the peak position of derivative magnetization

dM/dH . Combined the $M(H)$ and $M(T)$ curves, the H_{C2} is used to construct the field-temperature H - T phase diagram of $\text{Nd}_2\text{ZnIrO}_6$.

Reference

- [1] Pesin D and Balents L 2010 *Nat. Phys.* **6** 376
- [2] H. Takagi, T. Takayama, G. Jackeli, G. Khaliullin and S.E. Nagler 2019 *Nat. Rev. Phys.* **1** 264
- [3] Wan X G, Turner A M, Vishwanath A and Savrasov S Y 2011 *Phys. Rev. B* **83** 205102
- [4] Fang C, Lu L, Liu JW and Fu L, 2016 *Nat. Phys.* **12** 936
- [5] Chu H, Zhao L, De la Torre A, Hogan T, Wilson S D and Hsieh D 2017 *Nat. Mater.* **16** 200
- [6] Kim B J, Jin H, Moon S J, Kim J Y, Kim B G, Park B G, Leem C S, Yu J, Noh T M, Kim C, Oh S J, Park J H, Durairaj V, Cao G and Rotenberg E 2008 *Phys.Rev.Lett.* **101** 076402
- [7] Moretti Sala M, Ohgushi K, Al-Zein A, Hirata Y, Monaco G and Krisch M 2014 *Phys.Rev.Lett.* **112** 176402
- [8] Sheng J M, Ye F, Hoffmann C, Cooper V R, Okamoto S, Terzic J, Zheng H, Zhao H D and Cao G 2018 *Phys.Rev. B* **97** 235116
- [9] Qasim I, Kennedy B J and Avdeev M 2013 *J Mater. Chem. A* **42** 13357
- [10] Singh Y, Manni S, Reuther J, Berlijn T, Thomale R, Ku W, Trebst S and Gegenwart P 2012 *Phys. Rev. Lett.* **108** 127203
- [11] Rau J G, Lee E K and Kee H Y 2016 *Annu. Rev. Condens. Matter. Phys.* **7** 195
- [12] Okamoto Y, Nohara M, Aruga-Katori H and Takagi H 2007 *Phys. Rev. Lett.* **99** 137207
- [13] Matsuhira K, Wakeshima M, Hinatsu Y and Takagi S 2011 *J.Phys. Soc. Jpn.* **80** 094701
- [14] Cao G X, Subedi A, Calder S, Yan J Q, Yi J J, Gai Z, Poudel L, Singh D J, Lumsden M D, Christianson A D, Sales B C and Mandrus D 2013 *Phys. Rev. B* **87** 155136
- [15] Wakeshima M, Harada D, and Hinatsu Y 2000 *J. Mater. Chem.* **10** 419
- [16] Aczel A A, Clancy J P, Chen Q, Zhou H D, Reig-i-Plessis D, MacDougall G J, Ruff J P C, Upton M H, Islam Z, Williams T J, Calder S and Yan J Q 2019 *Phys. Rev. B* **99** 134417
- [17] Cook A M, Matern S, Hickey C, Aczel A A and Paramakanti A 2015 *Phys. Rev. B* **92** 020417
- [18] Aczel A A, Cook A M, Williams T J, Calder S, Christianson A D, Cao G X, Mandrus D, Kim Y B, and Paramakanti 2016 *Phys. Rev. B* **93** 214426
- [19] Mugavero III S J, Fox A H, Smith M D and Zur Loye H C 2010 *J. Solid. State. Chem.* **183** 465
- [20] Ferreira T, Morrison G, Yeon J and Zur Loye H C 2016 *Crystal Growth & Design* **16**

2795

- [21] Vogl M, Corredor L T, Dey T, Morrow R, Scaravaggi F, Wolter A U B, Aswartham S, Wurmehl S, and Buchner B 2018 *Phys. Rev. B* **97** 035155
- [22] Vogl M, Morrow R, Aczel A A, Rodriguez R B, Wolter A U B, Wurmehl S, Aswartham S, and Buchner B 2020 *Phys. Rev. Mater.* **4** 054413
- [23] Bandyopadhyay A, Carlomagno I, Simonelli L, Sala M M, Efimenko A, Meneghini C and Ray S 2019 *Phys. Rev. B* **100** 064416
- [24] Ghimire M P, Wu L H and Hu X 2016 *Phys. Rev. B* **93** 134421
- [25] Singh B, Vogl M, Wurmehl S, Aswartham S, Buchner B and Kumar P 2020 *Phys. Rev. Research* **2** 013040
- [26] Glazer A M 1972 *Acta Crystallogr. Sec. B* **28** 3384
- [27] Mott N F 1969 *Philos. Mag.* **19** 835
- [28] Kharkwal K C and Pramanik A K 2017 *J. Phys.: Condens. Matter.* **29** 495801
- [29] Cao H T, Liobet A, Barth J, Winterlik J, Felser C, Panthöfer M and Tremel W 2011 *Phys. Rev. B* **83** 134406
- [30] Lu L, Song M, Liu W, Reyes A P, Kuhns P, Lee H O, Fisher I R and Mitrović V F 2017 *Nat. Comm.* **8** 14407
- [31] S. Singh, S. Saha, S. K. Dhar, R. Suryanarayanan, A. K. Sood, and A. Revcolevschi 2008 *Phys. Rev. B* **77** 054408
- [32] Van Vleck J H 1927 *Phys. Rev. B* **29** 727
- [33] Ishikawa J J, O'Farrell E C T and Nakatsuji S 2012 *Phys. Rev. B* **85** 245109
- [34] Bothroyd A T, Doyle S M, Paul D M and Osborn R 1992 *Phys. Rev. B* **45** 10075
- [35] Singh B, Vogl M, Wurmehl S, Aswartham S, Buchner B and Kumar P 2020 *Phys. Rev. Research* **2** 023162
- [36] Makowski S J, Rodgers J A, Henry P F, Attfield J P and Bos J W G 2009 *Chem. Mater.* **21** 264
- [37] Gao Y X, Ashtar M, Xu L M, Ouyang Z W, Tong W, Yuan S L, Tian Z M 2020 *J. Phys.: Condens. Matter* **32** 105702
- [38] Wills A S, Zhitomirsky M E, Canals B, Sanchez J P, Bonville P, de Reotier P D and Yaouanc A 2006 *J. Phys.: Condens. Matter* **18** L37
- [39] Davis M J, Mugavero J S, Glab K I, Smith M D and zur Loye H C 2004 *Solid. Stat. Sci.* **6** 413
- [40] Tian Z M, Kohama Y, Tomita T, Ishizuka H, Hsieh T H, Ishikawa J I, Kindo K, Balents L and Nakatsuji S 2016 *Nat. Phys.* **12** 134
- [41] Chen G and Hermele M 2012 *Phys. Rev. B* **86** 235129
- [42] Fujita T C, Kozuka Y, Matsuno J, Uchida M, Tsukazaki A, Arima T and Kawasaki M 2018 *Phys. Rev. Mater.* **2** 011402

List of Tables

Table 1. The activation energy (Δ) fitted by the thermal activation model, and character temperature (T_0) by the VRH model for $\text{RE}_2\text{BIR}_2\text{O}_6$ (RE=La,Pr,Nd,Sm-Gd)

	La	Pr	Nd	Sm	Eu	Gd
$\Delta(\text{meV})$						
$\text{RE}_2\text{ZnIrO}_6$	336	386	417	425	460	517
$\text{RE}_2\text{MgIrO}_6$	382	388	415	462	518	562
$T_0^{1/4}(\text{K}^{1/4})$						
$\text{RE}_2\text{ZnIrO}_6$	126	131	137	139	153	166
$\text{RE}_2\text{MgIrO}_6$	127	124	137	146	161	173

Table 2. The magnetic parameters of $\text{RE}_2\text{BIR}_2\text{O}_6$ including magnetic ordering temperatures (T_C, T_N), Curie-Weiss temperature (θ_{CW}) and effective magnetic moment (μ_{eff}). The Curie-Weiss fitting is taken in temperature range (30 K-70 K) for $\text{Sm}_2\text{BIR}_2\text{O}_6$ and in temperature range (180 K -300 K) for $\text{RE}_2\text{BIR}_2\text{O}_6$ (RE=La,Pr,Nd, Eu, Gd; B=Zn,Mg).

$\text{RE}_2\text{BIR}_2\text{O}_6$	$T_N, T_C(\text{K})$	$\theta_{\text{CW}}(\text{K})$	$\mu_{\text{eff}}(\mu_{\text{B}}/\text{f.u.})$	$\mu_{\text{eff}} = \sqrt{2\mu_{\text{RE}}^2 + \mu_{\text{Ir}}^2}$ ($\mu_{\text{B}}/\text{f.u.}$)
B=Zn				
RE=La	8.4	-5.6	1.45	1.73
RE=Pr	12.0	-53.3	5.52	5.36 ^a
RE=Nd	15.4	-53.8	5.54	5.41 ^a
RE=Sm	13.2	-29.0	2.32	2.12 ^b
RE=Eu	11.0	9.4	1.51	1.73
RE=Gd	22.2	1.05	11.35	11.35 ^a
B=Mg				
RE=La	11.4	-19.0	1.52	1.73
RE=Pr	14.0	-49.0	5.42	5.36 ^a
RE=Nd	11.8	-51.3	5.32	5.41 ^a
RE=Sm	14.6	-48	2.25	2.12 ^b
RE=Eu	10.8	-15.3	1.53	1.73
RE=Gd	20.8	-5.4	11.35	11.35 ^a

^a $\mu_{\text{RE}} (\mu_{\text{B}})$ and $\mu_{\text{Ir}} (\mu_{\text{B}})$ are magnetic moments calculated by $g[J(J+1)]^{1/2}$ for free RE^{3+} ions and ideal $j_{\text{eff}}=1/2$ Ir^{4+} ions, ^b $\mu_{\text{RE}} (\mu_{\text{B}})$ is the Van Vleck PM moment ($0.85\mu_{\text{B}}$) per Sm^{3+} ion and $\mu_{\text{Ir}} (\mu_{\text{B}})$ is moment per Ir^{4+} ion.

Figure captions

Figure 1. (a) Crystal structure of double perovskite $\text{Pr}_2\text{ZnIrO}_6$, in which IrO_6 and ZnO_6 are drawn as octahedra. Dark cyan, orange and gray spheres correspond to Pr, Ir and Zn sites. (b,c) The local coordinated environments of magnetic Pr^{3+} and Ir^{4+} ions in the connection of distorted IrO_6 octahedra and PrO_8 polyhedron.

Figure 2. (a) The variation of Lattice parameters for $\text{RE}_2\text{ZnIrO}_6$ as a function of RE^{3+} ionic radius, (b) variation of RE-O/Ir-O bond lengths and tilting angle (ϕ) for $\text{RE}_2\text{ZnIrO}_6$ with ionic radius of RE^{3+} .

Figure 3. Temperature dependence of resistivity and fitting data for RE_2BlrO_6 series. (a,b) ρ versus T , (c,d) $\ln\rho$ versus T , the solid lines are fitted by thermal activation model. (e,f) $\ln\rho$ versus $T^{-1/4}$, the solid lines represent the fitting by VRH model.

Figure 4. (a-e) The ZFC and FC magnetic susceptibilities under $H=0.1$ T for RE_2BlrO_6 ($\text{RE}=\text{Pr}, \text{Nd}, \text{Sm}, \text{Eu}, \text{Gd}$), (f-j) the inverse susceptibilities of FC magnetizations for RE_2BlrO_6 , the black line shows the Curie-Weiss fitting. The inverse susceptibilities for Eu_2BlrO_6 are subtracted the Van Vleck PM parts.

Figure 5. (a) The isothermal $M(H)$ curves and (b) modified Arrot plot $(M)^{1/\beta}$ versus $(H/M)^{1/\gamma}$ for initial magnetizations of $\text{Eu}_2\text{ZnIrO}_6$, (c) Field dependent magnetization curves under pulsed magnetic fields at $T=2$ K for $\text{Eu}_2\text{ZnIrO}_6$, the magnetization value is calibrated by the DC magnetization data measured by SQUID.

Figure 6. (a) The isothermal $M(H)$ curves of $\text{Eu}_2\text{MgIrO}_6$, the dashed red line represents the linear extrapolation of high-field magnetizations (b) the derivative magnetization dM/dH curves for $\text{Eu}_2\text{MgIrO}_6$, (c) $M(T)$ curves at different fields for $\text{Eu}_2\text{MgIrO}_6$, the inset shows the dM/dT curves with $H=5$ T. (d) the constructed $H-T$ phase diagram based on the $M(H)$ and $M(T)$ data.

Figure 7. The isothermal $M(H)$ curves at different temperatures for (a) $\text{Gd}_2\text{ZnIrO}_6$ and (b) $\text{Gd}_2\text{MgTiO}_6$, respectively. The inset in (a) shows high field magnetizations at $T=2$ K for $\text{Gd}_2\text{ZnIrO}_6$, inset in (b) shows the dM/dH curves for $\text{Gd}_2\text{MgTiO}_6$, (c) $M(T)$ curves at different fields for $\text{Gd}_2\text{MgIrO}_6$, the inset shows the dM/dT curves at 1 T, (d) the $H-T$ phase diagram based on the $M(H)$ and $M(T)$ data.

Figure 8. The DC magnetization and pulsed field magnetization curves at 2 K for (a,b) Pr_2BlrO_6 , (c,d) Nd_2BlrO_6 and (e,f) Sm_2BlrO_6 , respectively. The dashed black lines in (a,c,f) show the linear magnetization extrapolations, the inset in (a,b,d) show the derivative magnetization dM/dH curves.

Figure 9. (a) The DC magnetization and (b) derivative magnetization dM/dH curves for $\text{Pr}_2\text{ZnIrO}_6$. (c) The pulsed field magnetization curves of $\text{Pr}_2\text{ZnIrO}_6$, inset shows the dM/dH curves (d) $M(T)$ curves at different fields for $\text{Pr}_2\text{ZnIrO}_6$, the inset shows the dM/dT curves

under $H=7$ T.

Figure 10. The constructed H - T phase diagrams based on the $M(H)$ and $M(T)$ data for (a) $\text{Pr}_2\text{ZnIrO}_6$ and (b) $\text{Nd}_2\text{ZnIrO}_6$. The diagram is composed of antiferromagnetic (AFM), canted-antiferromagnetic (C-AFM), polarized ferromagnetic state (PS) and paramagnetic (PM) regions.

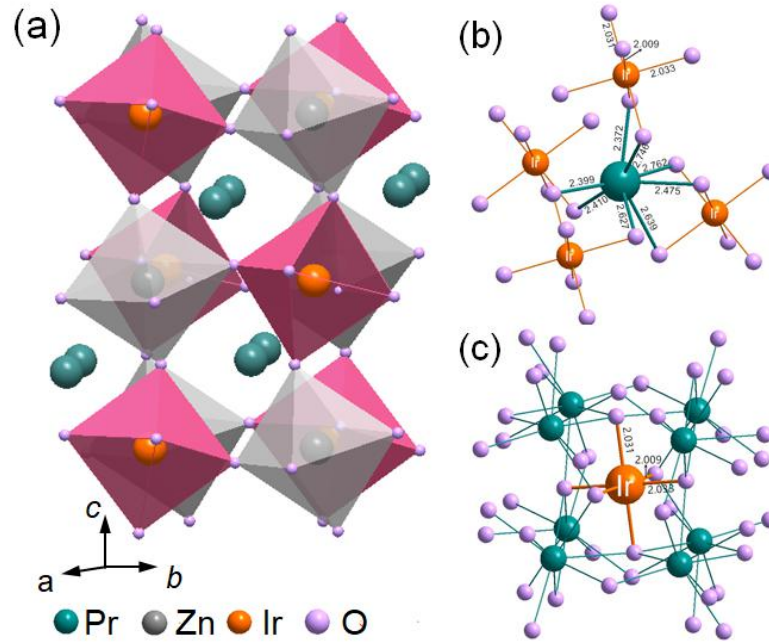


Figure 1

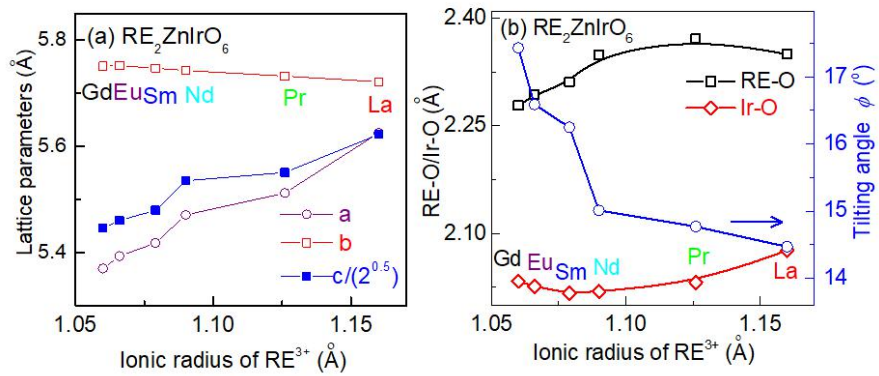


Figure 2

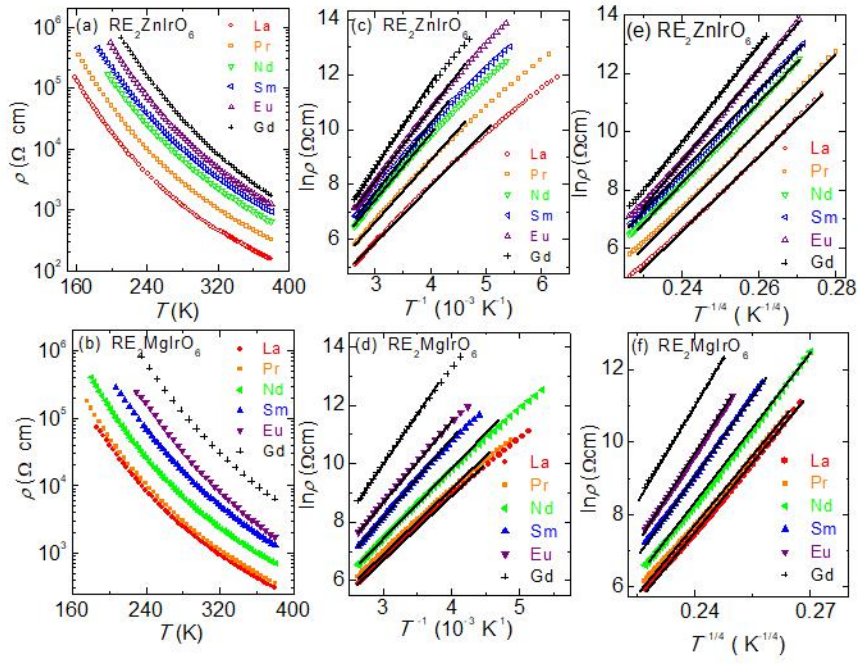


Figure 3

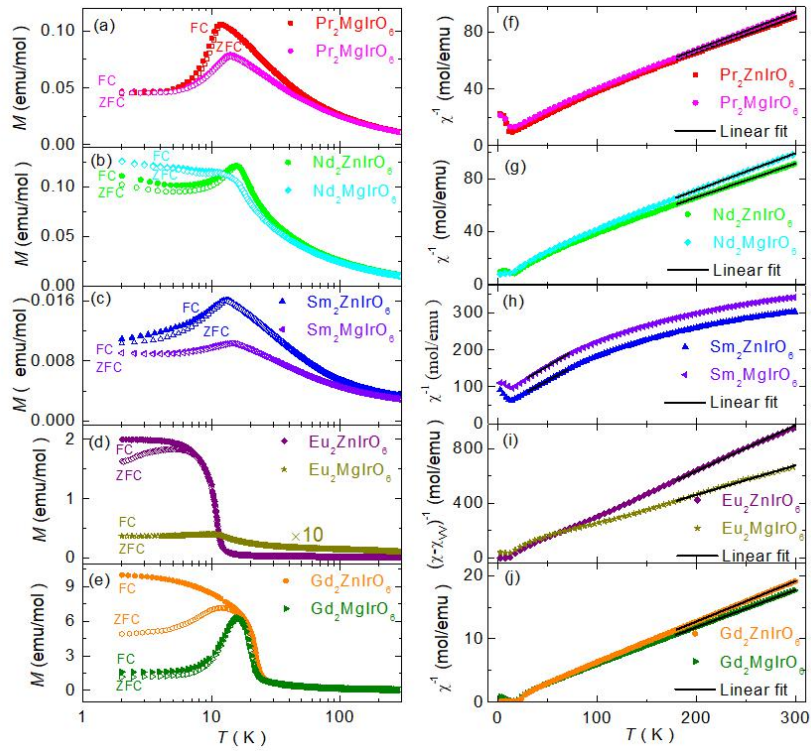


Figure 4

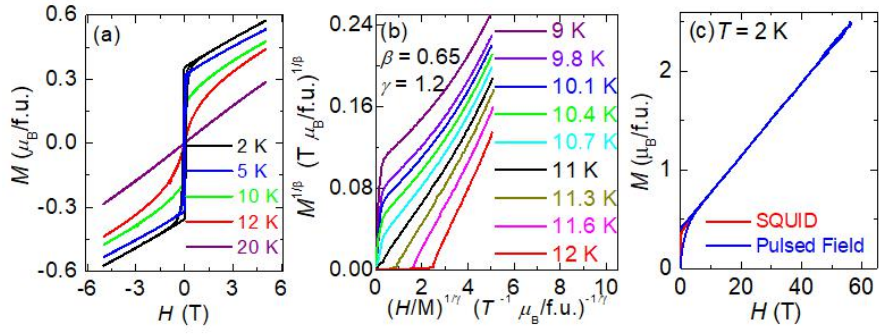


Figure 5

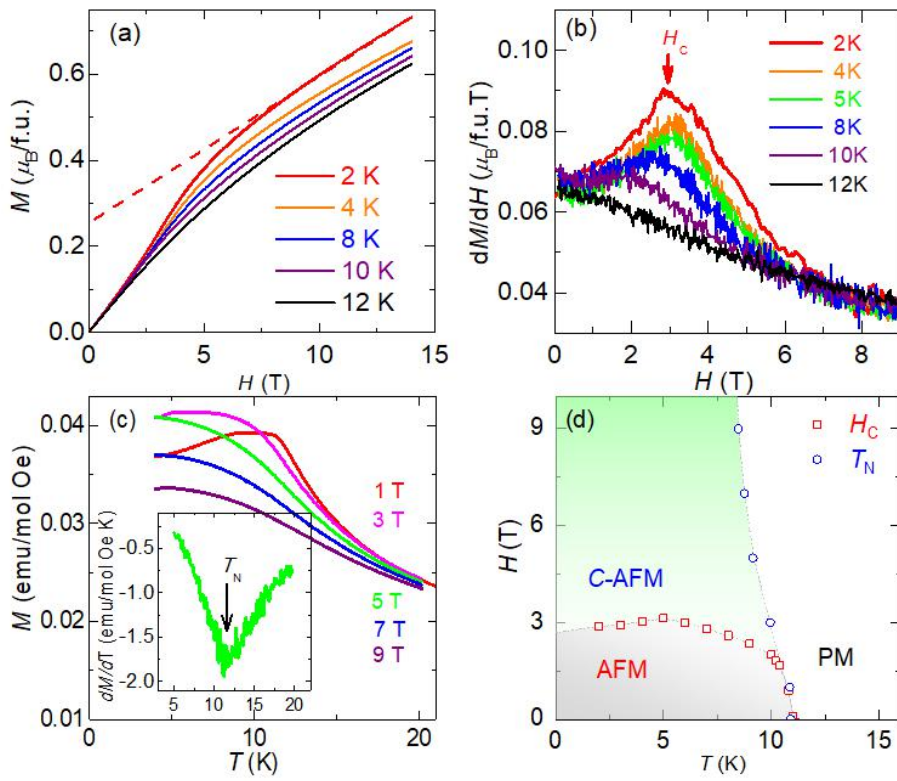


Figure 6

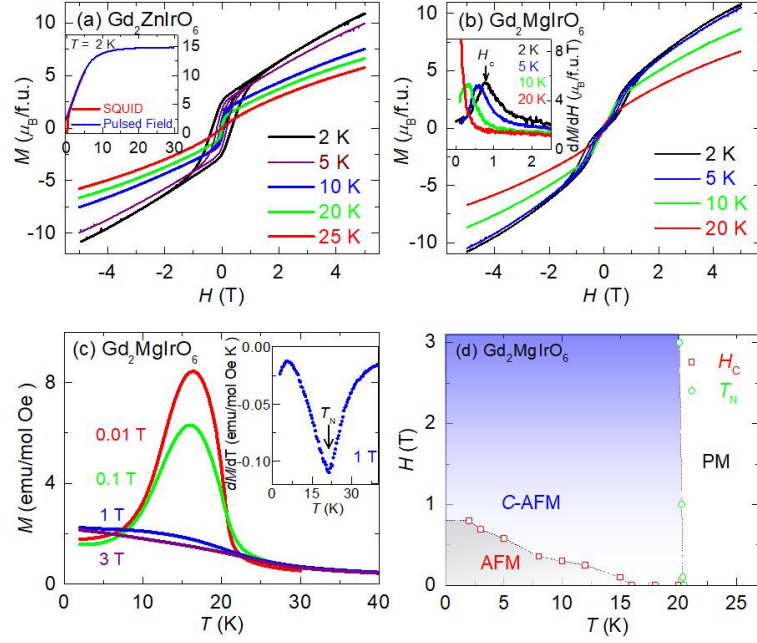


Figure 7

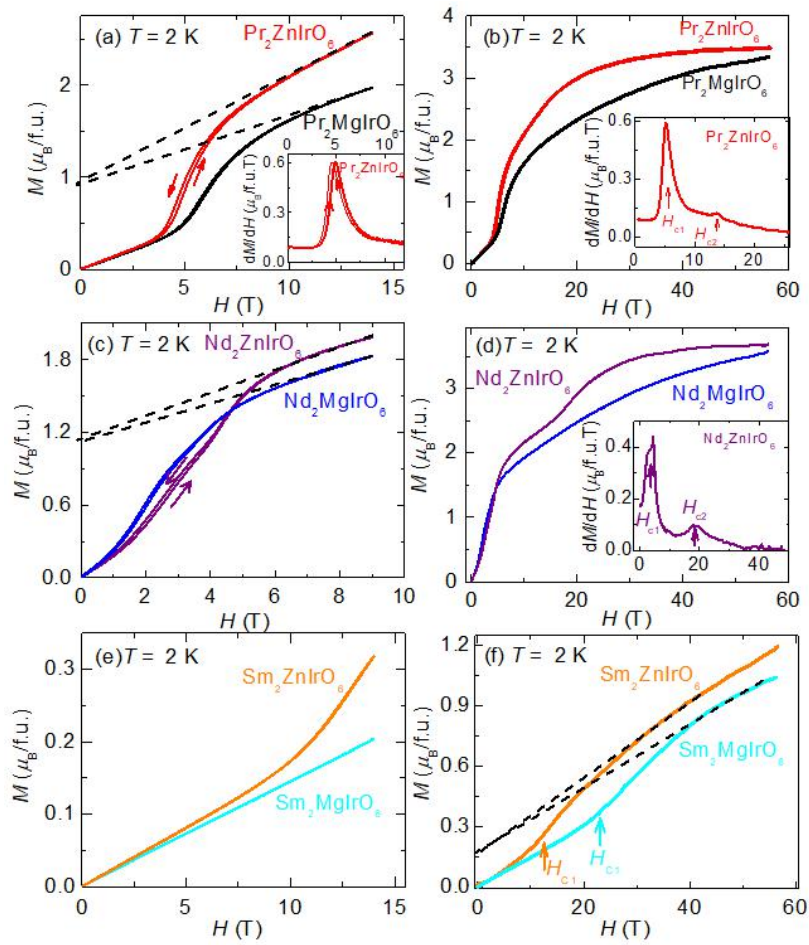


Figure 8

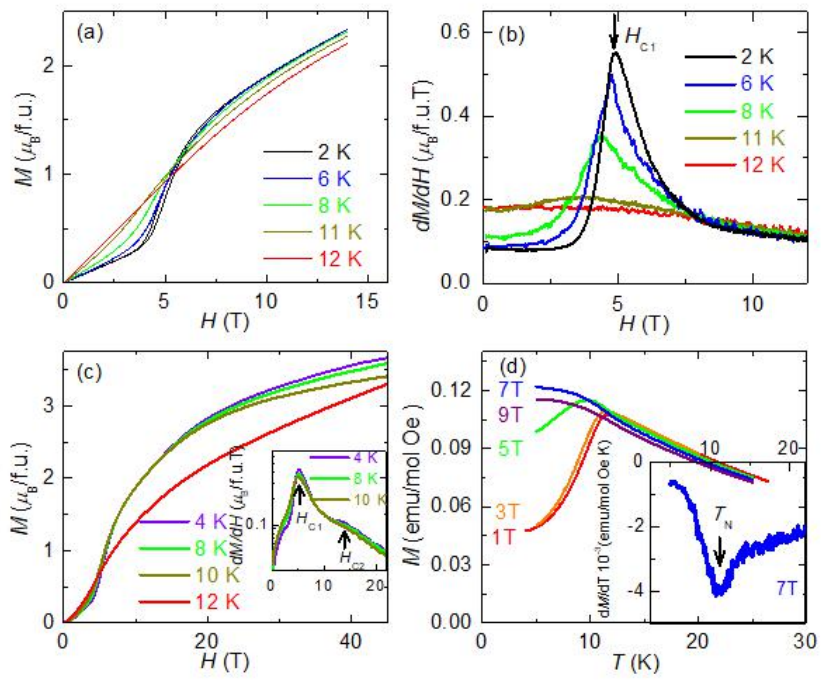


Figure 9

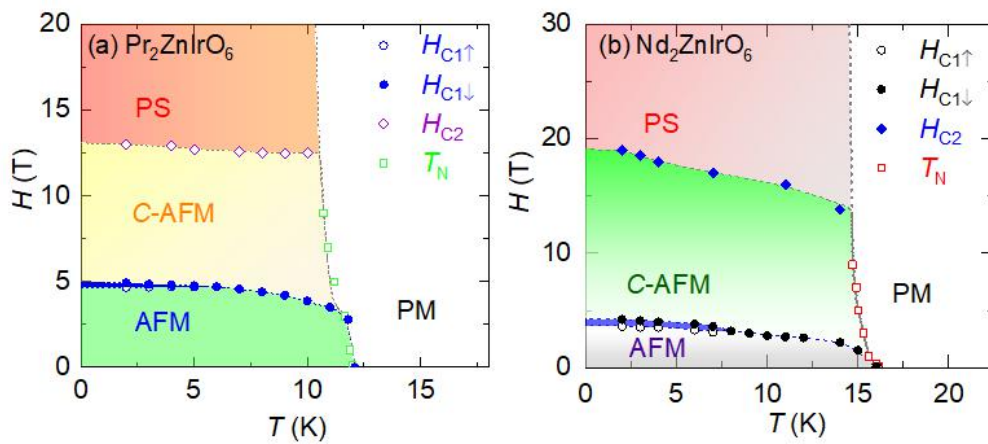


Figure 10